# Homoepitaxial Growth of Single Crystal Diamond Membranes for Quantum Information Processing

# Homoepitaxial Growth of Single Crystal Diamond Membranes for Quantum Information Processing

Igor Aharonovich[1*], Jonathan C. Lee[1*], Andrew P. Magyar[1], Bob B. Buckley[2], Christopher G. Yale[2], David D. Awschalom[2] and Evelyn L. Hu[1]

1. School of Engineering and Applied Sciences, Harvard University, MA 02138, USA
2. Center for Spintronics and Quantum Computation, University of California, Santa Barbara, California, 93106, USA

* Contributed equally to this work

igor@seas.harvard.edu

## Abstract

Fabrication of devices designed to fully harness the unique properties of quantum mechanics through their coupling to quantum bits (qubits) is a prominent goal in the field of quantum information processing (QIP). Among various qubit candidates, nitrogen vacancy (NV) centers in diamond have recently emerged as an outstanding platform for room temperature QIP. However, formidable challenges still remain in processing diamond and in the fabrication of thin diamond membranes, which are necessary for planar photonic device engineering. Here we demonstrate epitaxial growth of single crystal diamond membranes using a conventional microwave chemical vapor deposition (CVD) technique. The grown membranes, only a few hundred nanometers thick, show bright luminescence, excellent Raman signature and good NV center electronic spin coherence times. Microdisk cavities fabricated from these membranes exhibit quality factors of up to 3000, overlapping with NV center emission. Our methodology offers a scalable approach for diamond device fabrication for photonics, spintronics, optomechanics and sensing applications.

The exceptional properties of diamond, including a wide electronic and optical band gap, excellent thermal conductivity, and its biocompatibility are attractive for numerous optoelectronic and sensing applications[1-5]. One diamond color center in particular, the negatively charged nitrogen vacancy (NV) center, is among the most promising solid state qubits due to its room temperature operation, long spin coherence time, and suitability for optical initialization and readout[6]. Embedding color centers within a single crystal diamond membrane enables promising applications, including diamond-based QIP[7,8]. To this end, optically–active thin membranes are essential, as they are the fundamental building blocks of photonic components such as microcavities, photonic crystal cavities, resonators and waveguides.

Fabrication of planar devices often requires the material be undercut to achieve optical, electrical or mechanical isolation, as in the formation of mechanically-sensitive cantilever devices, optical microdisk cavities, or photonic crystal cavities[9-11]. Such structures are often formed by incorporating a sacrificial layer into the initial bulk material structure. Selective etch removal of the sacrificial layer can then create an undercut structure, or a larger membrane with thickness of 10's to 100's of nanometers, depending on the device application. However, such an approach is not available for creating undercut or membrane structures in diamond, as high quality hetero-epitaxy of single crystal diamond on dissimilar substrates has not yet been demonstrated due to lattice mismatches and low surface diffusion of carbon atoms[2,12,13].

An alternative technique has been employed for diamond: high energy (~ 1-3 MeV) and high dose ion implantation (~ $1\times10^{17}$ ions/cm$^2$) generates a thin amorphous layer below the diamond surface that can be selectively etched leaving behind a diamond membrane several hundred nanometers in thickness[14-19]. Nevertheless, poor spin coherence properties, weak luminescence from its color centers, and a residual built-in strain as a result of the high ion damage significantly limit the performance of diamond membranes fabricated in this manner. Indeed, no working optical cavities, spin measurements or devices have been demonstrated from ion-damaged diamond membranes to date.

To address this challenge, we introduce an approach that utilizes the diamond membranes as templates for the epitaxial overgrowth of a thin layer of single crystal diamond. Growth is carried out in a Plasma-Enhanced Chemical Vapor Deposition (PECVD)

reactor and results in single crystal diamond layers with superior physical, optical, and spin properties than their original diamond templates. Furthermore, the overgrowth process allows us to intentionally dope the diamond device layer with color centers such as NV or silicon-vacancy (SiV) centers that were *not present* in the original diamond template. Indeed, strong luminescence, narrow Raman peaks and the appearance of NV center spin lifetimes in the membrane, are characteristic of a high quality bulk diamond. After growth, the diamond template can be completely etch-removed, leaving the highest quality overgrown diamond membrane to be further formed into device structures. The schematic of the process is depicted in Fig. 1a. The specific homoepitaxial growth conditions were: microwave power 950 W, pressure 60 torr under 400 standard cubic centimeters per minute of 99:1 $CH_4/H_2$.

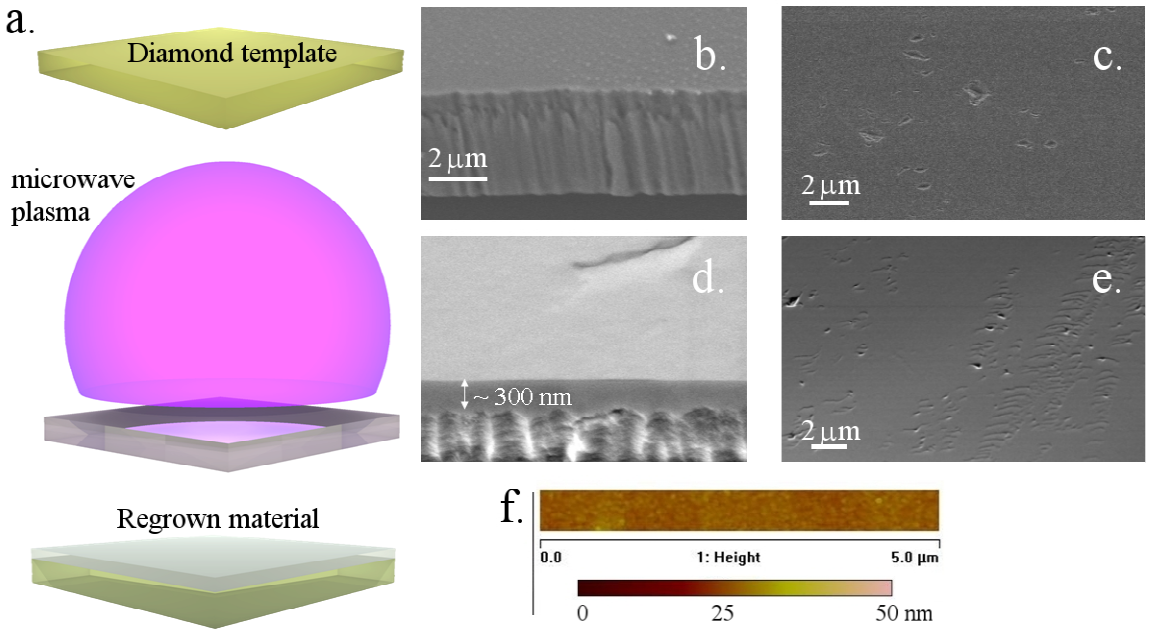


**Figure 1. Diamond membrane growth and surface properties. a.** Schematic illustration of the regrowth process of the diamond membrane using a PECVD reactor. **b.** SEM side view and **c.** top view of the original diamond membrane before the regrowth. **d.** SEM side view and **e.** top view showing a ~ 300 nm overgrowth of a single crystal diamond. The pits observed on the surface are transferred from the original membrane. **f.** AFM scan of a 5 μm strip demonstrating the smoothness of the top membrane surface. The surface roughness is measured to be 4 nm.

Fig. 1b,c show the top view and the cross sectional scanning electron microscope (SEM) images of the original membrane, 1.7 μm in thickness. Fig. 1d,e illustrate the overgrown

material after 5 minutes of growth. The single crystal material, with a top (100) facet, is clearly observed on top of the original membrane. No indications of polycrystalline material, grain boundaries or surface defects (e.g. hillocks) are observed. The pits in the regrown layer are transferred from the original membrane, which was pitted. In principle, this can be avoided through the use of smooth, dislocation free, single crystal diamond as a starting material. Importantly, the undamaged regions of the regrown material are very smooth. Atomic force microscope (AFM) scans reveal that the root mean square (RMS) surface roughness is only 4 nm (Fig. 1d). In comparison, the RMS surface roughness of a typical commercially available CVD single crystal diamond is on the order of 2-3 nm.

Raman spectroscopy can provide detailed information about the structural quality of a material. The best diamond templates show Raman peaks at 1331 $cm^{-1}$ with a FWHM of 9.9 $cm^{-1}$ (after removing the most damaged region but before any annealing or regrowth treatment). For comparison, the Raman peak we measure for bulk single crystal diamond is centered at 1333.5 $cm^{-1}$ with a FWHM of 2.3 $cm^{-1}$. Remarkably, the Raman signature of the composite overgrown membrane-plus-template gave a peak value of 1332 $cm^{-1}$ with a FWHM of 6.6 $cm^{-1}$. These values are a convolution of the Raman peak from the overgrown material with that of the membrane template, and accounts for the best fit to two peaks, shown in Fig. 2a.

To further gauge the influence of the template quality on the properties of the overgrown diamond, material was overgrown on the most heavily-damaged surface of the template (which was *not* removed by etching) (Fig. 2b)[18]. Even with a heavily damaged template material, the epitaxially grown material exhibits superior Raman characteristics with linewidth of ~ 3 $cm^{-1}$, approaching the quality of a bulk single crystal diamond, despite the shifted and much broader Raman signature of the template, as seen in the green curve of Fig. 2b. This is convincing evidence that the overgrown diamond film has excellent structural properties, and that the residual strain in the template material does not propagate into the overgrown material[20].

Despite the fact that a highly damaged diamond membrane with a high strain field was used as a template, the overgrown material exhibits excellent lattice properties. This is contrary to conventional epitaxial growth of other semiconductors (e.g. GaAs) where the

strain in the template is manifested in the properties of the overgrown material and often reduces its quality[21].

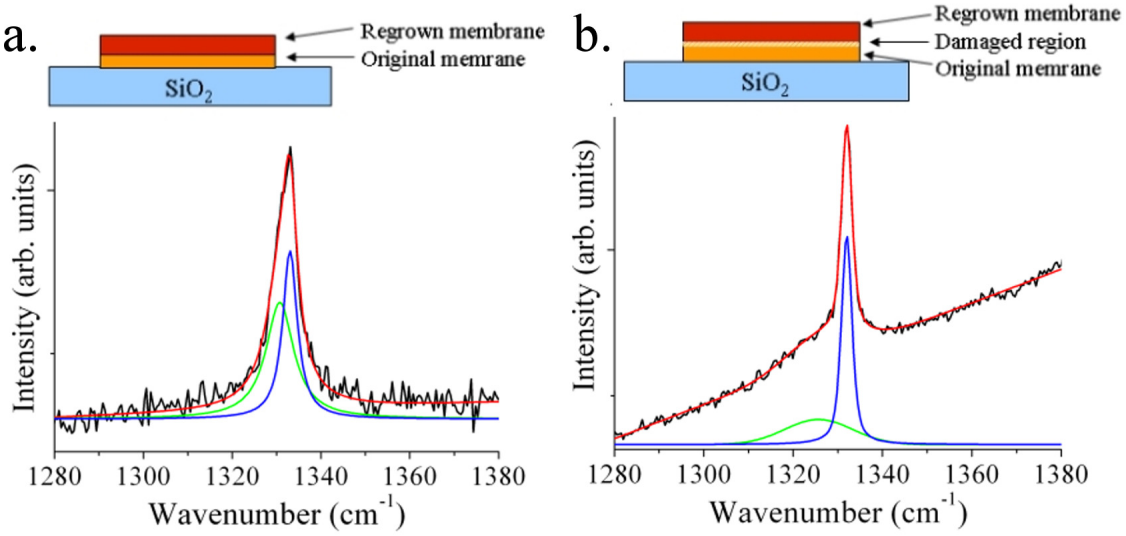


**Figure 2**. **Raman studies of the epitaxially-grown membrane. a.** Diamond membrane grown on a lifted-off diamond slab with the damaged side etched away. The double Voigt fitting of the Raman line (red curve) reveals a FWHM of ~ 4 $cm^{-1}$ for the regrown material (blue curve) and ~ 7 $cm^{-1}$ for the original membrane (green curve). **b.** Diamond membrane growth on the damaged side of the lifted-off membrane. Despite the damaged original material with a wide Raman line (green curve, FWHM of ~ 17 $cm^{-1}$), the regrown material shows a much narrower FWHM of ~ 3 $cm^{-1}$ for the regrown material (blue curve).

To further investigate the optical properties of the regrown material, photoluminescence (PL) measurements were recorded under 532 nm excitation at room temperature. The regrown membranes showed bright fluorescence even though the original templates were not optically active. The appearance of PL clearly indicates that the formation of color centers occurs during the CVD growth, offering an exceptional opportunity to engineer on demand color centers in the overgrown diamond membranes. We have demonstrated this by engineering two types of different membranes – one with primarily NV centers and the other with SiV centers. Fig. 3 shows the photoluminescence (PL) recorded from two different regrown membranes – one with primarily NV centers (a) while the second one has mainly SiV defects. To control the impurity incorporation, the membranes are positioned on various substrates. For instance, for the incorporation of the SiV defect, the membrane was placed on a silicon dioxide substrate. We further note that other defects

(e.g. oxygen vacancy) may exist in our membranes. However, they are not optically active within the investigated spectra range (~550-900 nm)

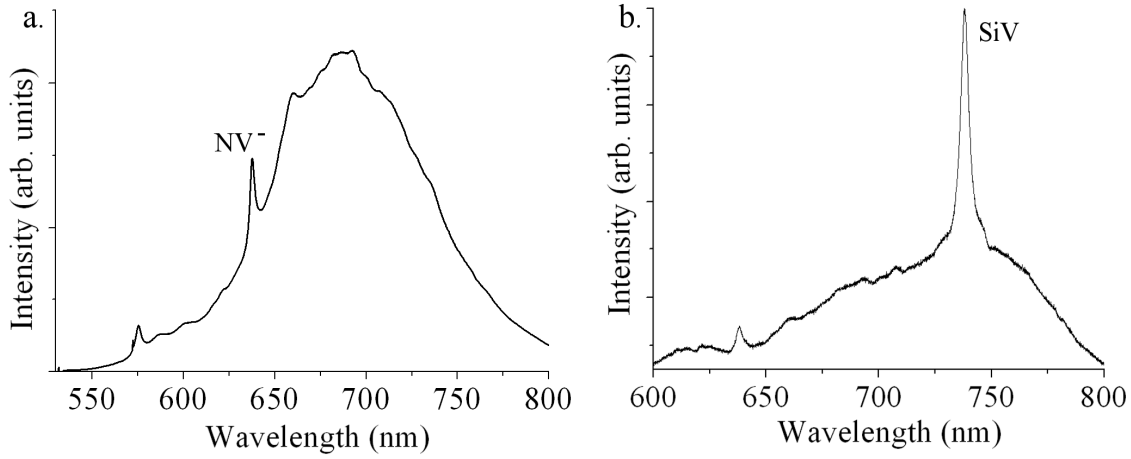


**Figure 3. Optical characteristics of the regrown template.** (a) PL spectrum recorded from an overgrown membrane, with dominating NV concentration. (b) PL spectrum recorded from a different overgrown membrane, showing primarily the SiV defects.

The impurity incorporation can be controlled by placing the template on various substrates, e.g. silicon, sapphire or other bulk diamond. We believe that during the growth, the plasma slightly etches the substrate, whose elements are subsequently incorporated into the growing diamond lattice[22].

Some of the most promising scientific and technological applications of diamond are spin-based QIP algorithms[4,5] and detection of weak magnetic fields with high sensitivity[23-26]. For these, an important prerequisite is characterizing the coherent dynamics of the NV center electron spin. We note that no electron spin resonance signal was detected from the original diamond templates prior to the regrowth process. After the epitaxial regrowth of membranes containing NV centers, an optically detected magnetic resonance (ODMR) signal was observed, motivating further investigation of the NV center spin properties within the grown membranes.

Figure 4 plots various measures of ensemble spin coherence as functions of time at room temperature and with no applied magnetic field. More details regarding the timing sequences to determine these measures can be found in the supplemental material. In Fig. 4a, the NV center longitudinal spin coherence as a function of time is plotted. Fitting to

an exponential decay reveals a spin-lattice relaxation time of $T_1$ = 5 ms for the NV center ensemble. The transverse homogeneous spin coherence, plotted in Fig. 4b, was measured with a Hahn echo sequence and was found to have a value of $T_2$ = 3.5 μs when fit to a single exponential decay. Fig. 4c plots the transverse inhomogeneous spin coherence, taken with a Ramsey sequence (off resonance by ~ 25 MHz). The pronounced beating in the Ramsey data suggests several distinct spin resonance frequencies which may be due to crystal strain energetically splitting the $S_X$ and $S_Y$ spin sublevels as well as a small stray magnetic field. A fit consisting of a single exponential decay envelope around four beating frequencies reveals $T_2^*$=158 ns for this ensemble of NV centers. It should be noted that transverse spin coherence is sensitive to the surrounding spin bath, originating from the presence of other electron and nuclear spins as well as magnetic fluctuations on the surface. The measured values of $T_2$ and $T_2^*$ for the regrown material are comparable with shallow implanted NVs in a bulk diamond[27] and are higher than typical coherence times found in nanodiamonds[28].

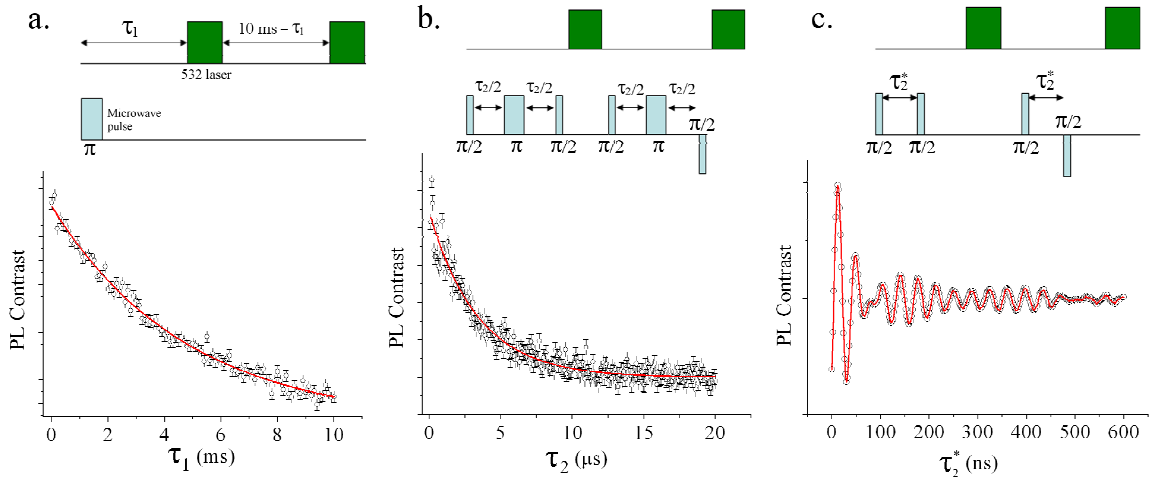


**Figure 4. Coherence properties of the grown membrane. a.** Spin lattice relaxation time, yielding $T_1$ ~ 5 ms. The red curve is a single exponential fit of the data. **b.** Hahn-echo sequence of the transverse homogeneous spin coherence time resulting with a $T_2$ ~ 3.5 μs. The red curve is a single exponential fit of the data. **c.** Ramsey sequence to determine transverse inhomogeneous spin coherence precession decay time, yielding $T_2^*$ ~ 158 ns. Error bars are smaller than data markers. The sequences applied to measure the spin properties are schematically depicted. All the data are recorded at room temperature with no applied magnetic field.

Remarkably, good spin behavior exists in the regrown material despite the fact that the original template did not show any ODMR signal and the regrown membrane is only a few hundred nanometers thick. The spin properties of the regrown membrane further confirm the high quality of the thin, single crystal diamond membrane and indicate promise for applications in nano-magnetometry and QIP.

The spin properties of the regrown diamond membranes can be significantly improved by growing the membrane with $^{12}C$ isotopically purified methane, as the nuclear spin of $^{13}C$ can significantly reduce the NV spin coherence[6]. Additional experimental steps such as high temperature annealing[29] can also be applied to boost the coherence of the embedded NV centers.

A number of reasons can account for the successful growth of high quality single crystal diamond membranes. First, a uniform diffusion of atomic hydrogen and methyl radicals on the surface of the diamond template enables uniform progression of the diamond growth. Such uniformity is achieved partly due to the small size of the membrane compared to the size of the plasma ball (even at 950 W). In addition, using lower power, and hence a lower temperature results in a reduced mobility of the carbon species, preventing both nucleation on surface defects and the formation of hillocks or nanodiamonds. Indeed, when the plasma density is increased, many more nucleation sites are formed on the membrane and square helices can be observed. Fig. 5 shows regrowth on the membrane under non-optimal growth conditions. In Fig. 5a a high temperature causes fast nucleation with many individual nanodiamond nuclei. The clusters then coalesce into a polycrystalline film. In Fig. 5b the membrane was positioned further away from the plasma ball, reducing effectively the plasma density and the etching rate in a vicinity of the membrane. This results in non-homogeneous nucleation of larger individual diamond crystals. The above results stress the importance of the correct growth conditions for high quality single crystalline diamond membranes. It is further clear that only a narrow window of experimental conditions must be used to grow a single crystal diamond layer.

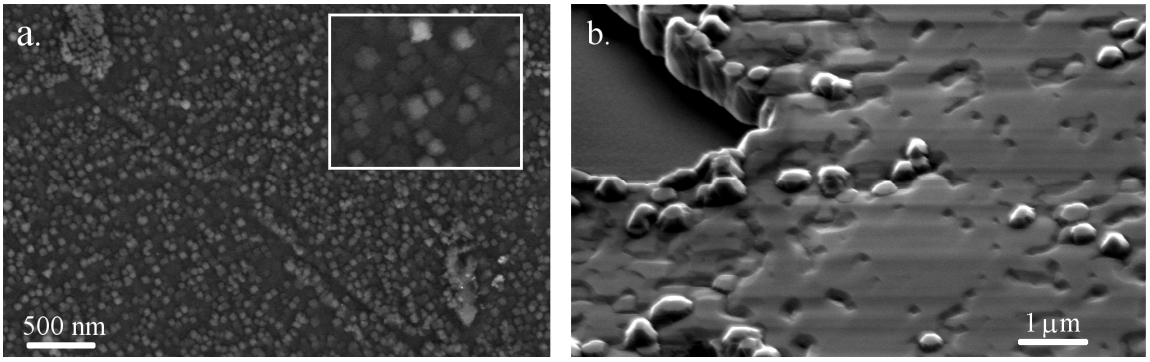


**Figure 5. SEM images of inhomogeneous nucleation on the diamond template.** (a) SEM image of the regrown material under high temperature conditions. (b) SEM image of the regrown material at lower plasma density. In both cases there is inhomogeneous nucleation that hinders the single crystal membrane formation.

We note that our growth conditions are not typical of those used for homoepitaxial, single crystal diamond growth, which often requires higher microwave power densities (~ 2 – 4 kW) and higher pressure (~ 150 – 250 torr)[30,31].

Having at our disposal an optically-active, thin, single crystal diamond membrane, we demonstrate its suitability for QIP by fabricating an optical microcavity. Fig. 6a shows PL spectra recorded from this microdisk (black curve) and the substrate (red curve) at room temperature. The NV zero phonon line (ZPL) is visible at 637 nm. The peaks decorating the PL recorded from the microdisk are the modes with quality factors (Q) ~ 1500. Q's of up to 3000 were measured from the microdisk cavities. Figure 6b shows a typical SEM image of a microdisk cavity (diameter of 2.5 μm and a thickness of ~ 800 nm), fabricated from the epitaxially-grown membrane.

In conclusion, we have described a process that produces thin, optically-active, high-quality single crystal diamond membranes. The regrowth results are intriguing for a number of reasons. First, an improved Raman signature indicates a much smaller strain distribution in the regrown membranes. This is despite the fact that the original templates are structurally imperfect with high strain fields. Second, the regrown material exhibits good spin properties, unlike the original template which did not exhibit any spin signature. Third, the regrowth methodology allows engineering of other color centers within the regrown material. Further exploration of the growth conditions could lead towards thin single crystal diamond membranes with a low distribution of color centers

that can emit single photons on demand (e.g. NV, SiV, Cr) – an important prerequisite for single photon device engineering.

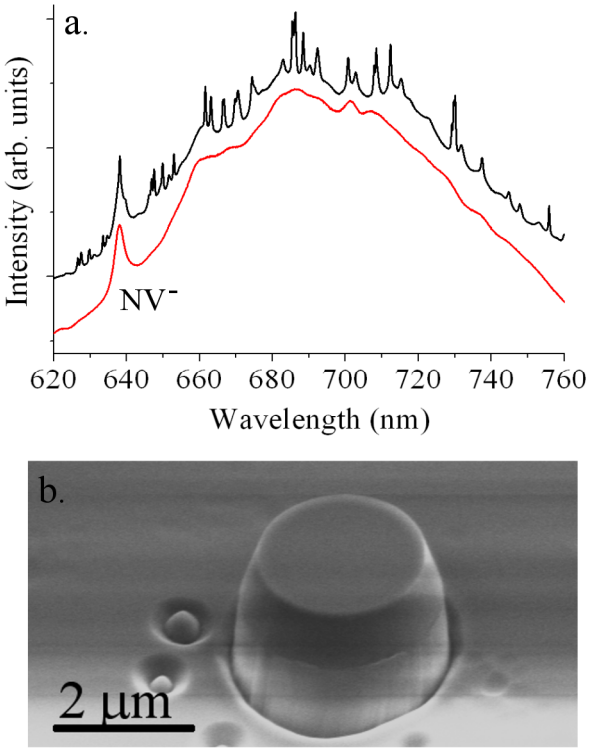


**Figure 6. Diamond microdisk cavity fabricated from the regrown membrane. a.** PL spectra recorded from the diamond membrane (red curve) and from a 1 µm microdisk (black curve, shifted for clarity) under 532 nm excitation at room temperature. The ZPL of the NV center is clearly seen at 637 nm. The spectrum from the microdisk is decorated with modes with typical $Q \sim 1500$. **b.** A typical SEM image of a microdisk cavity with a diameter of 2.5 mm and a thickness of ~ 800 nm.

The successful homoepitaxial growth of thin diamond membranes is a pivotal step in advancing diamond processing. Our results provide important insights that can potentially further the understanding of the complicated diamond CVD growth, particularly its nucleation steps. The demonstration of high quality epitaxial diamond growth even on damaged diamond template opens new avenues towards engineering of thin, high quality, single diamond membranes. The scalability of this process can propel the use of diamond from laboratory setting into a plethora of devices spanning high power electronics, photonics, sensing and QIP.

**Acknowledgments**

The authors thank Prof David Clarke for the access to the Raman facilities, F.J. Heremans and A.L. Falk for the assistance with the optical measurements, M. Huang for the assistance with ion implantation. The authors also acknowledge A. Yacoby, M. Grinolds, S. Hong and P. Maletinsky for the assisting with the initial ESR measurements and thank T.M. Babinec for useful discussions.

**References**

1 Ladd, T. D., Jelezko, F., Laflamme, R., Nakamura, Y., Monroe, C. & O'Brien, J. L. Quantum computers. *Nature* **464**, 45-53, (2010).

2 Balmer, R. S. *et al.* Chemical vapour deposition synthetic diamond: materials, technology and applications. *J. Phys.: Condens. Matter* **21**, 364221, (2009).

3 Aharonovich, I., Greentree, A. D. & Prawer, S. Diamond photonics. *Nature Photon.* **5**, 397-405, (2011).

4 Awschalom, D. D., Epstein, R. & Hanson, R. The diamond age of spintronics - Quantum electronic devices that harness the spins of electrons might one day enable room-temperature quantum computers - made of diamond. *Sci. Am.* **297**, 84, (2007).

5 Neumann, P. *et al.* Quantum register based on coupled electron spins in a room-temperature solid. *Nature Phys.* **6**, 249-253, (2010).

6 Balasubramanian, G. *et al.* Ultralong spin coherence time in isotopically engineered diamond. *Nature Mater.* **8**, 383-387, (2009).

7 Faraon, A., Barclay, P. E., Santori, C., Fu, K. M. & Beausoleil, R. G. Resonant enhancement of the zero-phonon emission from a colour centre in a diamond cavity. *Nature Photon.*, (2011).

8 Santori, C., Barclay, P. E., Fu, K. M. C., Beausoleil, R. G., Spillane, S. & Fisch, M. Nanophotonics for quantum optics using nitrogen-vacancy centers in diamond. *Nanotech* **21**, 274008, (2010).

9 Gavartin, E. *et al.* Optomechanical Coupling in a Two-Dimensional Photonic Crystal Defect Cavity. *Phys. Rev. Lett.* **106**, (2011).

10 Eichenfield, M., Chan, J., Camacho, R. M., Vahala, K. J. & Painter, O. Optomechanical crystals. *Nature* **462**, 78-82, (2009).

11 Vahala, K. J. Optical microcavities. *Nature* **424**, 839-846, (2003).

12 Butler, J. E., Mankelevich, Y. A., Cheesman, A., Ma, J. & Ashfold, M. N. R. Understanding the chemical vapor deposition of diamond: recent progress. *J. Phys.: Condens. Matter* **21**, (2009).

13 Schreck, M., Hormann, F., Roll, H., Lindner, J. K. N. & Stritzker, B. Diamond nucleation on iridium buffer layers and subsequent textured growth: A route for the realization of single-crystal diamond films. *Appl. Phys. Lett.* **78**, 192-194, (2001).

14 Parikh, N. R. *et al.* Single-crystal diamond plate liftoff achieved by ion-implantation and subsequent annealing. *Appl. Phys. Lett.* **61**, 3124-3126, (1992).

15 Fairchild, B. A. *et al.* Fabrication of Ultrathin Single-Crystal Diamond Membranes. *Adv. Mater.* **20**, 4793, (2008).
16 Bayn, I., Meyler, B., Salzman, J. & Kalish, R. Triangular nanobeam photonic cavities in single-crystal diamond. *New J. Phys.* **13**, (2011).
17 Babinec, T. M., Choy, J. T., Smith, K. J. M., Khan, M. & Loncar, M. Design and focused ion beam fabrication of single crystal diamond nanobeam cavities. *J. Vac. Sci. Technol. B* **29**, (2011).
18 Magyar, A. *et al.* Fabrication of Thin, Luminescent, Single-crystal Diamond Membranes. *Appl. Phys. Lett.* **99**, 081913, (2011).
19 Marchywka, M., Pehrsson, P. E., Vestyck, D. J. & Moses, D. Low-energy ion-implantation and electrochemical separation of diamond films. *Appl. Phys. Lett.* **63**, 3521, (1993).
20 *Note that small strain fields are present in the grown template as is evident by the ODMR measurements described in the text. We believe that these are strain fields characteristic of any CVD-grown diamond and are negligible compared to the highly damaged material whose strain is characterized by substantial Raman shifts.*
21 Stangl, J., Holy, V. & Bauer, G. Structural properties of self-organized semiconductor nanostructures. *Rev. Mod. Phys.* **76**, 725-783, (2004).
22 Aharonovich, I., Zhou, C. Y., Stacey, A., Treussart, F., Roch, J. F. & Prawer, S. Formation of color centers in nanodiamonds by plasma assisted diffusion of impurities from the growth substrate. *Appl. Phys. Lett.* **93**, 243112, (2008).
23 Balasubramanian, G. *et al.* Nanoscale imaging magnetometry with diamond spins under ambient conditions. *Nature* **455**, 648-652, (2008).
24 Maze, J. R. *et al.* Nanoscale magnetic sensing with an individual electronic spin in diamond. *Nature* **455**, 644-648, (2008).
25 de Lange, G., Wang, Z. H., Riste, D., Dobrovitski, V. V. & Hanson, R. Universal Dynamical Decoupling of a Single Solid-State Spin from a Spin Bath. *Science* **330**, 60-63, (2010).
26 Grinolds, M. S., Maletinsky, P., Hong, S., Lukin, M. D., Walsworth, R. L. & Yacoby, A. Quantum control of proximal spins using nanoscale magnetic resonance imaging. *Nature Phys.* **7**, 687-692, (2011).
27 Toyli, D. M., Weis, C. D., Fuchs, G. D., Schenkel, T. & Awschalom, D. D. Chip-Scale Nanofabrication of Single Spins and Spin Arrays in Diamond. *Nano Lett.* **10**, 3168-3172, (2010).
28 Baranov, P. G. *et al.* Enormously High Concentrations of Fluorescent Nitrogen-Vacancy Centers Fabricated by Sintering of Detonation Nanodiamonds. *Small* **7**, 1533-1537, (2011).
29 Naydenov, B. *et al.* Increasing the coherence time of single electron spins in diamond by high temperature annealing. *Appl. Phys. Lett.* **97**, 242511 (2010).
30 Martineau, P. M. *et al.* High crystalline quality single crystal chemical vapour deposition diamond. *J. Phys.: Condens. Matter* **21**, 8, (2009).
31 Achard, J. *et al.* High quality MPACVD diamond single crystal growth: high microwave power density regime. *J. Phys. D: Appl. Phys.* **40**, 6175-6188, (2007).

**Supplementary Information**

**Generation of initial diamond templates –** A type IIA CVD diamond crystal (Element Six) was implanted with He ions (1 MeV, $5\times10^{16}$ He/cm$^2$) and annealed for one hour at 900$^\circ$ C. The sample was then immersed in water, and using electrochemical etching carried out under constant voltage, the membranes were lifted off and placed on different substrates.

**Regrowth process –** the original single crystal diamond membranes were first cleaned using a mixed (1:1:1 sulfuric – perchloric – nitric acid) and put into a Seki Technotron AX5010-INT PECVD reactor. The chamber was evacuated below 0.1 mtorr and flushed with $H_2$ gas. The homoepitaxial growth conditions were: microwave power 950 W, pressure 60 torr, 400 SCCM of 99:1 $CH_4/H_2$ for 5 minutes. No external heating source was used.

**Device fabrication** – the regrown membranes were flipped and thinned down using oxygen inductive coupled plasma reactive ion etching (ICP-RIE) to their final thickness of ~ 500 nm. A silicon dioxide hard mask was deposited on top of the membranes and the microdisk cavities were patterned using e-beam lithography and etched down using ICP-RIE.

**Spectroscopy** – the Raman data was collected using 532 nm laser excitation with a conventional confocal Raman microscope (LabRAM ARAMIS, Horiba Jobin-Yvon) at room temperature. The typical spatial resolution of the microscope is ~ 1 μm.

The PL measurements were recorded using a custom built confocal microscope using a 532 nm continuous wave (CW) diode laser through a 100×, 0.9 numerical aperture objective. The emission was collected through the same objective and directed into a spectrometer. The laser light was filtered using a dichroic mirror.

**Spin coherence measurements** – The samples were placed in a confocal microscopy setup with a 100× objective where a 532 nm laser for photoexcitation, microwave magnetic fields for spin manipulation, and the sample PL measured by an avalanche photodiode were all gated in time for time-domain spin coherence measurements. Timing sequences for the measurements of $T_1$, $T_2$, and $T_2^*$ (see supplemental material) were generated by an arbitrary waveform generator.

**Spin Coherence Sequences**

The timing sequence (Fig. 4a) to determine the longitudinal spin coherence time ($T_1$) consists of an initialization 532 nm laser pulse of 5 μs, followed by a single microwave magnetic field pulse whose frequency is resonant with the NV center's $S_Z$-$S_X$ spin transition. This microwave "π" pulse flips the NV centers electronic spin state from $S_Z$ to $S_X$. The ensemble spin state is then measured with a second 532 nm "readout" laser pulse via PL intensity. The measurement is performed as a function of delay time ($\tau_1$) between the initialization and readout 532 nm laser pulses. To normalize the PL and determine the spin contrast between $S_Z$ and $S_X$, the resulting PL is subtracted from a similar sequence without the spin-flipping microwave π pulse. The resulting subtracted data is plotted in Fig. 4a as a function of time. A single exponential decay fit of this subtracted data determines a $T_1$ time of 5.00 ± 0.07 ms.

The transverse homogeneous spin coherence time is determined by the following timing sequence (Fig. 4b). The spin is first initialized into $S_Z$ with an initialization pulse of 3 μs. Then, a Hahn echo sequence which uses microwave magnetic field pulses resonant with the $S_Z$-$S_X$ NV center spin transition was applied. The Hahn echo begins with a π/2 microwave pulse which rotates the spins onto the equator of the Bloch sphere. This is followed by a π pulse after a time $\tau_2/2$. The final π/2 pulse, a time $\tau_2/2$ after the π pulse, flips the spins back to the poles of the Bloch sphere for spin readout. Finally, the ensemble spin state is read out via PL using a second 532 nm "readout" laser pulse. The free precession time, $\tau_2$, is varied. To compensate for pulse errors, the center π pulse is 90° out of phase from the π/2 pulses. The spin contrast is plotted in Fig. 4b as the difference in PL intensity between flipping and not flipping the sign of the final π/2 microwave pulse relative to the initial π/2 pulse. Fitting this subtracted data to a single exponential decay determines $T_2 = 3.46 \pm 0.07$ μs.

Finally, the transverse inhomogeneous spin coherence time is determined with a Ramsey timing sequence (Fig. 4c). Once again, the spin is initialized into $S_Z$ with a laser pulse of 3 μs. The Ramsey sequence consists of two π/2 pulses separated by a time $\tau_2^*$, which is varied. Like the Hahn echo sequence, the spin contrast is the difference in PL intensity between whether the sign of the last π/2 pulse is flipped or not, relative to the initial π/2

pulse. Ramsey sequences are typically performed with a detuned microwave frequency, and in this sequence, the microwaves are detuned by 25 MHz from the $S_X$ resonance in order to induce oscillations in the data. We see beating of four frequencies (two frequencies per spin resonance peak), which suggests a small magnetic field or asymmetric strain may play a role in splitting the spin sublevels of differing orientations of NV centers. The data, plotted in Fig. 4c, is fit to four beating frequencies with a single exponential decay envelope,

$$I = y_0 + e^{-t/T_2^*}(A_{1a}\cos(2\pi(\omega_1 + a)t + \phi_1) + (A_{1b}\cos(2\pi(\omega_1 - a)t + \phi_1)$$
$$+ (A_{2a}\cos(2\pi(\omega_2 + a)t + \phi_2) + (A_{2b}\cos(2\pi(\omega_2 - a)t + \phi_2))$$

where $I$ is the PL contrast; $y_0$ is an offset; $T_2$* is the decay envelope time; $A_{1a}$, $A_{1b}$, $A_{2a}$, $A_{2b}$ are amplitudes; $\phi_1$ and $\phi_2$ are fixed phases; $\omega_1$ and $\omega_2$ are the two strain split spin sublevel energies (offset by the ~25 MHz detuning), and $2a$ is the magnetic field induced splitting. The $T_2^*$ time is determined to be 158.5 ± 1.5 ns.

For completeness, the other parameters in the fit are determined to be:

| Fitting Parameters | Values |
|---|---|
| $y_0$ | -4717 ± 306 cts |
| $T_2^*$ | 158.5 ± 1.5 ns |
| $A_{1a}$ | 239734 ± 3828 cts |
| $A_{1b}$ | 121048 ± 1806 cts |
| $A_{2a}$ | -114904 ± 1800 cts |
| $A_{2b}$ | -229847 ± 3785 cts |
| $\phi_1$ | -2.71 ± .01 |
| $\phi_2$ | 1.55 ± .01 |
| $\omega_1$ | 24.99 ± .01 MHz |
| $\omega_2$ | 29.59 ± .01 MHz |
| $a$ | 1.03 ± .01 MHz |